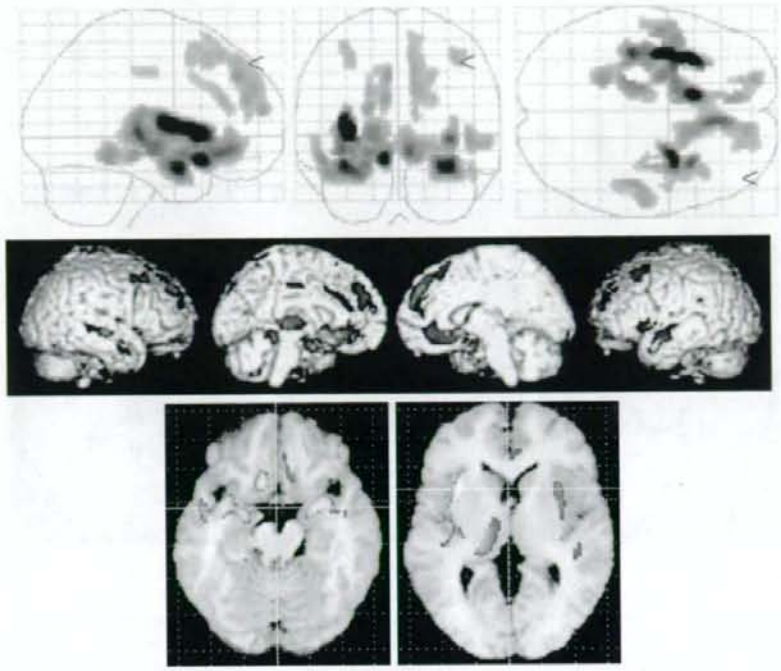

Fig. 3 Decreased volumes in schizophrenics ($n = 47$) as compared to controls ($n = 76$). *Top*: The SPM {*t*} is displayed in a standard format as a maximum-intensity projection (MIP) viewed from the right, the back and the top of the brain. The anatomical space corresponds to the atlas of Talairach and Tournoux. Representation in stereotaxic space of regions with significant reduction of volume in schizophrenia was demonstrated. Schizophrenics demonstrated a significant reduction of volumes in the multiple brain areas, such as the limbic and paralimbic systems, neocortical areas and the subcortical regions. *Middle*: The SPM {*t*} is rendered onto T_1-weighted MR images. *Bottom*: The SPM {*t*} is displayed onto axial T_1-weighted MR images. A significantly decreased volume of the amygdala-uncus, bilateral insular cortices, ACC, temporal cortex and the left thalamus in schizophrenics was noted.

In the limbic and paralimbic systems, patients with schizophrenia showed reduction of volumes in the parahippocampal gyri, amygdala-uncus, insular cortices and the anterior cingulate cortices (ACC). They also demonstrated reduced volumes in the frontal and temporal association areas, dorsal premotor areas and the left thalamus. In comparison with controls, patients with schizophrenia showed significantly increased volume in the CSF space such as lateral ventricle, sylvian and the interhemispheric fissures but not in the grey matter (Table 2 and Fig. 4).

Morphological changes associated with the Val158Met polymorphism (genotype effects)

In comparison with Met-COMT carriers, individuals homozygous for the Val-COMT allele demonstrated a significant reduction of volumes in the left ACC and the right middle temporal gyrus (MTG) (Table 2 and Fig. 5). The hypothesis-driven analysis demonstrated a genotype effect on volumes in the bilateral DLPFC (right BA9, left BA8) at a lenient threshold (uncorrected $P = 0.05$) (data are not shown), however, no voxels could survive after the correction for multiple comparisons (FDR < 0.05) within the ROI. There were no areas that individuals homozygous for the Val-COMT allele demonstrated a significant increment of volume compared to Met-COMT carriers.

Genotype—diagnosis interaction effects

We found significant genotype-diagnosis interaction effects on brain morphology. The stronger effects of Val158Met polymorphism on brain morphology in schizophrenia than those in controls were noted in the left ACC and the left amygdala-uncus (Table 2 and Fig. 6). The hypothesis-driven analysis demonstrated a genotype-diagnosis interaction effect on the volume of the right DLPFC (BA9/46) at a lenient threshold (uncorrected $P = 0.05$) (data not shown), however, no voxels could survive after the correction of multiple comparisons (FDR < 0.05) within the ROI.

Effects of the Val58Met polymorphism on brain morphology

Since genotype–disease interaction effects were found, we estimated the effects of genotypes on brain morphology in the control groups and the schizophrenic groups separately.

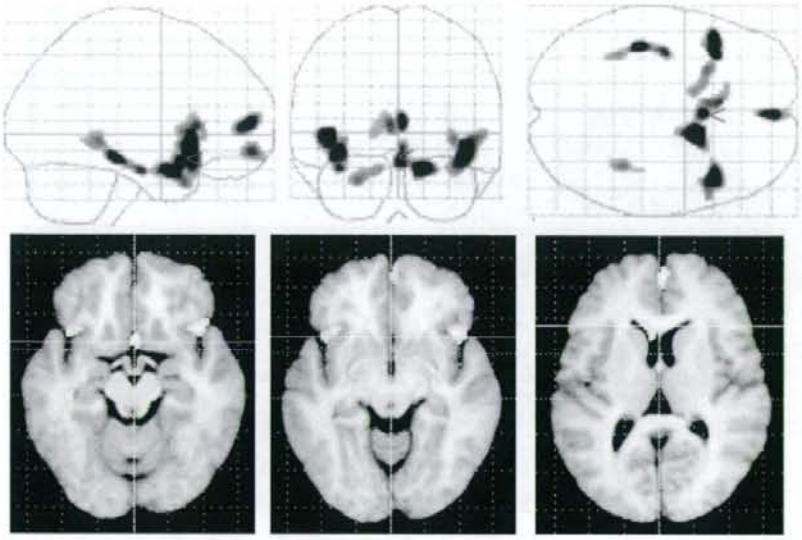

Fig. 4 Increased volumes in schizophrenics as compared to controls. *Top*: The SPM {*t*} is displayed in a standard format as a MIP. Patients with schizophrenia showed a significantly increased volume of the CSF space. *Bottom*: The SPM {*t*} is displayed onto axial T_1-weighted MR images. A significantly increased volume of the CSF space such as the lateral ventricle, sylvian fissures and the interhemisphrenic fissure was noted.

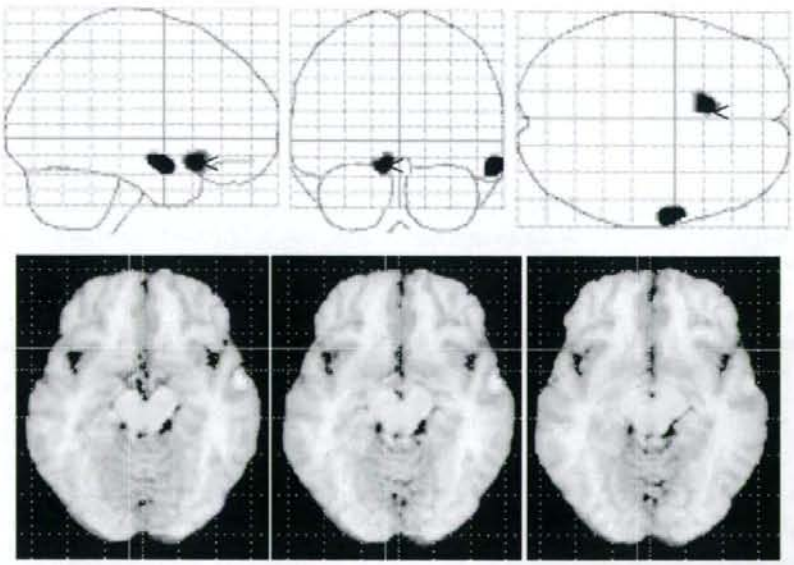

Fig. 5 The result of comparison between individuals homozygous for the Val-COMT allele (n = 57) and Met-COMT carriers (n = 66) (genotype effects). *Top*: Representation in stereotaxic space of regions with significant reduction of volume in individuals homozygous for the Val-COMT allele demonstrated. *Bottom*: The SPM {*t*} is displayed onto axial T_1-weighted MR images. Individuals homozygous for the Val-COMT allele demonstrated a significant reduction of volumes in the left ACC and right MTG as compared to Met-COMT carriers.

In the control group, we found no significant morphological differences between individuals homozygous for the Val-COMT allele and Met-COMT carriers. Even the hypothesis driven analysis with a lenient statistical threshold ($P < 0.05$) could not detect any significant morphological changes in the DLPFC between the two groups. Contrary to the control group, schizophrenics homozygous for the Val-COMT allele showed a significant reduction of volumes in the left amygdala-uncus, bilateral ACC, right MTG and the left thalamus when compared to the patients carrying the Met-COMT

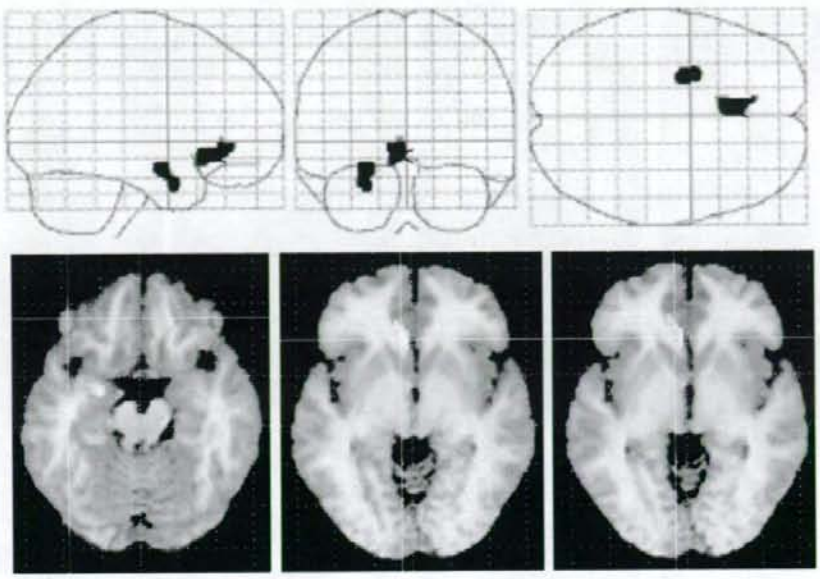

Fig. 6 Results of genotype-diagnosis interaction effects on brain morphology. *Top*: The SPM {*t*} is displayed in a standard format as a MIP. The stronger effects of Val158Met polymorphism on brain morphology in schizophrenia than those in controls were noted in the left ACC, left parahippocampal gyrus and the amygdala-uncus. *Bottom*: The SPM {*t*} is displayed onto axial T_1-weighted MR images.

allele (Table 2, Fig. 7). The hypothesis-driven analysis demonstrated a significantly decreased volume of the bilateral DLPFC in schizophrenics homozygous for the Val-COMT allele when compared to the Met-COMT schizophrenics at a lenient threshold (uncorrected $P = 0.05$) (data not shown). However, no voxels could survive after the correction for multiple comparisons (FDR < 0.05) within the ROI. There are no significantly increased volumes in the schizophrenics homozygous for the Val-COMT allele. All the results were essentially unchanged even if all the left-handed subjects were excluded in all analyses (data not shown).

Discussion

In this study, we found reduction of volumes in the limbic and paralimbic systems, neocortical areas (prefrontal and temporal cortices) and thalamus in patients with schizophrenia when compared to control subjects. The schizophrenia patients demonstrated a significant enlargement of CSF spaces including the lateral and sylvian fissure, which could be interpreted as a result of impaired neurodevelopment and/or global brain atrophy. These findings are concordant with previous studies of MR morphometry of schizophrenia. According to a recent review and meta-analyses of the morphometry of schizophrenia, the consistent abnormalities in schizophrenia are as follows; (i) ventricular enlargement (lateral and third ventricles); (ii) medial temporal lobe involvement; (iii) superior temporal gyrus involvement (iv) parietal lobe involvement; and (v) subcortical brain region involvement including the thalamus (Okubo *et al.*, 2001; Shenton *et al.*, 2001; Davidson and Heinrichs, 2003). The other regions observed in this study, such as the insula, DLPFC and the ACC have also often been demonstrated as abnormal areas in schizophrenia (Shenton *et al.*, 2001; Takahashi *et al.*, 2004; Yamasue *et al.*, 2004). Using the TBM technique, we replicated the morphological abnormalities observed in previous MR studies on schizophrenia, suggesting that TBM was able to detect morphological changes associated with this disease. As well as neuroimaging studies, post-mortem studies have also reported morphological abnormalities in schizophrenia, but not necessarily as common neuropathological features. Regions including the hippocampus, ACC, thalamus and the DLPFC are regularly associated with abnormalities of cell size, cell number and neuronal organization (Bogerts, 1993; Arnold and Trojanowski, 1996; Selemon, 2001; Selemon and Lynn, 2002, 2003). Selemon *et al.* reported that schizophrenics demonstrated abnormalities in overall and laminar neuronal density in the DLPFC (Brodmann area 9) and suggested that the DLPFC should be a particularly vulnerable target in the disease process (Selemon 2001; Selemon and Lynn, 2002, 2003).

Importantly, our results suggest that some of the morphological changes in schizophrenia mentioned above are associated with the Val158Met polymorphism of the COMT gene. In the schizophrenic group, the polymorphism was associated with the volumes in the limbic and paralimbic systems, temporal cortices and the left thalamus, whereas no morphological changes related to the polymorphism were found in

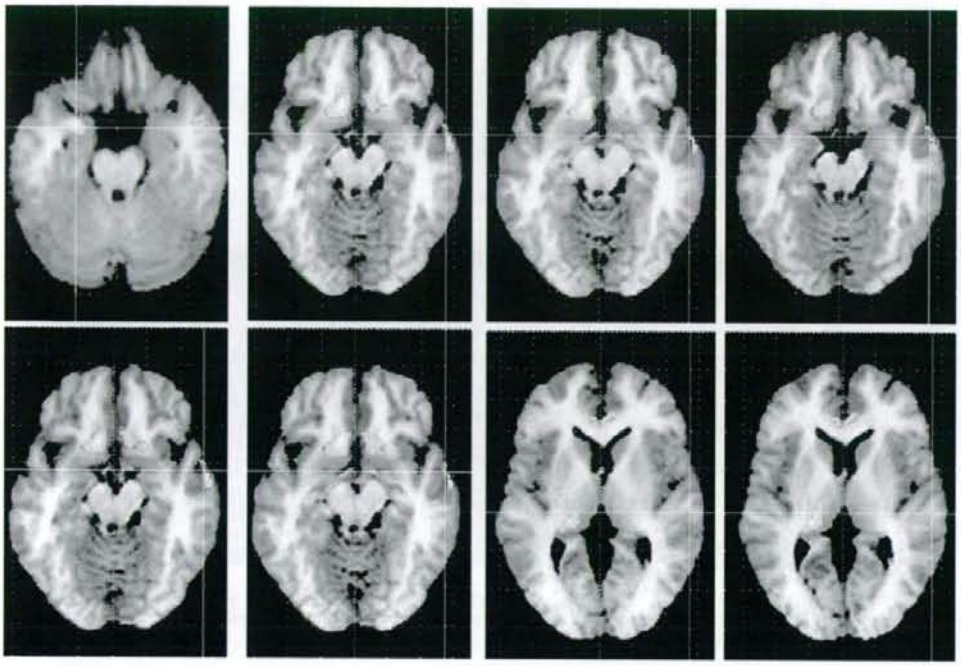

Fig. 7 The effects of the Val158Met polymorphism of the COMT gene on brain morphology in schizophrenics. The SPM {*t*} is displayed onto axial T_1-weighted MR images. The schizophrenics homozygous for the Val-COMT allele (n = 19) showed a significant reduction of volumes in the left parahippocampal gyrus, amygdala-uncus, ACC, left thalamus and the right MTG when compared to patients who carried the Met-COMT allele (n = 28).

normal individuals. As a consequence, significant genotype-diagnosis interaction effects were found in the left ACC and the amygdala-uncus. These results indicate that the Val158-Met polymorphism of the COMT gene is strongly associated with morphological changes in schizophrenia, particularly those in the limbic and paralimbic systems. Longitudinal MRI studies of schizophrenia strongly suggest that progressive changes should occur after onset of the illness (Okubo *et al.*, 2001; Ho *et al.*, 2003). Recent studies have demonstrated that antipsychotic drugs, particularly haloperidol, have considerable effects on brain morphology (Arango *et al.*, 2003; Lieberman, 2005; Dorph *et al.*, 2005). Because of the long duration of illness and medication taken by our subjects, the effects of antipsychotics may be a possible confounding factor for our findings. However, the duration of medication and the dose of antipsychotics taken by the Val/Val-COMT schizophrenics did not differ from those of the Met-COMT schizophrenics. Although the effects of antipsychotics on brain morphology may contribute to the observed morphological changes in patients with schizophrenia in this study, it is unlikely that the effects of antipsychotics contributed to morphological differences between the two schizophrenic groups.

When we were preparing this manuscript, another study demonstrated no genotype and genotype-diagnosis interaction effects of the Val158Met polymorphism on morphology of the frontal lobe in controls and schizophrenia (Ho *et al.*, 2005). Although there are differences between the two studies, such as mean ages of subjects, duration of illness, methods for image analysis and a racial factor (Caucasians versus Japanese), that study also demonstrated no genotype and genotype-diagnosis interaction effects on morphology of the DLPFC. However, we found these effects on DLPFC morphology at a very lenient statistical threshold. Further studies with a larger sample will clarify whether Val158Met polymorphism does affect DLPFC morphology. As well as prefrontal morphology, we found no significant genotype or genotype-diagnosis interaction effects on working memory, however, schizophrenics homozygous for the Val-COMT allele tended to have poorer performances on working memory measures, compared to Met-COMT carriers with schizophrenia. Although there were no significant effects of Val158Met polymorphism on working memory and other neuropsychological measures, a significant effect of the polymorphism was noted in brain morphology. The brain morphology has been considered to be useful as an intermediate phenotype in genetic research in neuropsychiatric disorders (Baare *et al.*, 2001; Durston *et al.*, 2005). Therefore, morphological changes might be more sensitive to the effects of genotype than behavioural measures such as the performance of working memory measures. In a previous study (Ho *et al.*, 2005) a similar phenomenon—no significant effect of Val158Met polymorphism on working memory performance but significant

effects on brain activities during a working memory task—was found. Further studies with a larger sample size are needed to clarify whether morphological changes are a more sensitive marker of genotype effects than behavioural measures.

Unexpectedly, we found effects of the polymorphism on the ACC volume rather than the DLPFC which is crucial for working memory. Since the ACC is associated with a variety of cognitive tasks involving mental efforts, and also plays important roles in working memory (Paus *et al.*, 2001; Kondo *et al.*, 2004), it is feasible that the Val158Met polymorphism may be associated with the ACC morphology. In fact, a previous study demonstrated that the Val-COMT allele was associated with abnormal ACC function as well as abnormal prefrontal cortical function, relative to the Met-COMT allele, as measured by cognitive tests and fMRI activation in normal subjects (Egan *et al.*, 2001).

One would argue that the effects of one polymorphism of the gene could not explain the morphological changes in schizophrenia. As well as the effects of the Val158Met polymorphism, we agree that other polymorphisms of schizophrenia susceptibility genes and genotype–genotype interaction may relate to individual brain morphology. Such interactions might contribute to the different effects of the Val158Met polymorphism on brain morphology observed in this study. Further studies of each effect and interaction of several schizophrenia susceptibility genes on brain morphology, brain functions and performances of neuropsychological tests should be conducted to clarify how polymorphisms of these genes affect intermediate phenotypes of schizophrenia.

In conclusion, we found an association between the Val158Met polymorphism and morphological abnormalities in schizophrenia. Although the underlying mechanisms of our observation remain to be clarified, our data indicate that brain morphology as an intermediate phenotype should be useful for investigating how genotypes affect endophenotypes of schizophrenia.

Acknowledgements

This study was supported by the Promotion of Fundamental Studies in Health Science of Organization for Pharmaceuticals and Medical Devices Agency. This work was also supported in part by Grants-in-Aid from the Japanese Ministry of Health, Labor and Welfare (H17-kokoro-007 and H16-kokoro-002), the Japanese Ministry of Education, Culture, Sports, Science and Technology and Core research for Evolutional Science and Technology of Japan Science and Technology Agency, Japan Foundation for Neuroscience and Mental Health.

References

Arango C, Breier A, McMahon R, Carpenter WT Jr, Buchanan RW. The relationship of clozapine and haloperidol treatment response to prefrontal, hippocampal, and caudate brain volumes. Am J Psychiatry 2003; 160: 1421–7.

Arnold SE, Trojanowski JQ. Recent advances in defining the neuropathology of schizophrenia. Acta Neuropathol (Berl) 1996; 92: 217–31.

Ashburner J, Friston KJ. High-dimensional image warping. In: Frackowiak R, editor. Human brain function. 2nd edn. Academic Press; 2004. p. 673–94.

Baare WF, Hulshoff Pol HE, Boomsma DI, Posthuma D, de Geus EJ, Schnack HG, et al. Quantitative genetic modeling of variation in human brain morphology. Cereb Cortex 2001; 11: 816–24.

Bogerts B. Recent advances in the neuropathology of schizophrenia. Schizophr Bull 1993; 19: 431–45.

Cannon TD, Mednick SA, Parnas J, Schulsinger F, Praestholm J, Vestergaard A. Developmental brain abnormalities in the offspring of schizophrenic mothers. I. Contributions of genetic and perinatal factors. Arch Gen Psychiatry 1993; 50: 551–64.

Chen J, Lipska BK, Halim N, Ma QD, Matsumoto M, Melhem S, et al. Functional analysis of genetic variation in catechol-O-methyltransferase (COMT): effects on mRNA, protein, and enzyme activity in postmortem human brain. Am J Hum Genet 2004; 75: 807–21.

Daniels JK, Williams NM, Williams J, Jones LA, Cardno AG, Murphy KC, et al. No evidence for allelic association between schizophrenia and a polymorphism determining high or low catechol O-methyltransferase activity. Am J Psychiatry 1996; 153: 268–70.

Davidson LL, Heinrichs RW. Quantification of frontal and temporal lobe brain-imaging findings in schizophrenia: a meta-analysis. Psychiatry Res 2003; 122: 69–87.

Dorph Petersen KA, Pierri JN, Perel JM, Sun Z, Sampson AR, Lewis DA. The influence of chronic exposure to antipsychotic medications on brain size before and after tissue fixation: a comparison of haloperidol and olanzapine in macaque monkeys. Neuropsychopharmacology 2005; 30: 1649–61.

Durston S, Fossella JA, Casey BJ, Hulshoff Pol HE, Galvan A, Schnack HG, et al. Differential effects of DRD4 and DAT1 genotype on fronto-striatal gray matter volumes in a sample of subjects with attention deficit hyperactivity disorder, their unaffected siblings, and controls. Mol Psychiatry 2005; 10: 678–85.

Egan MF, Goldberg TE, Kolachana BS, Callicott JH, Mazzanti CM, Straub RE, et al. Effect of COMT Val108/158 Met genotype on frontal lobe function and risk for schizophrenia. Proc Natl Acad Sci USA 2001; 98: 6917–22.

Fan JB, Zhang CS, Gu NF, Li XW, Sun WW, Wang HY, et al. Catechol-O-methyltransferase gene Val/Met functional polymorphism and risk of schizophrenia: a large-scale association study plus meta-analysis. Biol Psychiatry 2005; 57: 139–44.

Galderisi S, Maj M, Kirkpatrick B, Piccardi P, Mucci A, Invernizzi G, et al. COMT Val(158)Met and BDNF C(270) T polymorphisms in schizophrenia: a case-control study. Schizophr Res 2005; 73: 27–30.

Gaser C, Nenadic I, Buchsbaum BR, Hazlett EA, Buchsbaum MS. Deformation-based morphometry and its relation to conventional volumetry of brain lateral ventricles in MRI. Neuroimage 2001; 13: 1140–5.

Gogtay N, Sporn A, Clasen LS, Greenstein D, Giedd JN, Lenane M, et al. Structural brain MRI abnormalities in healthy siblings of patients with childhood-onset schizophrenia. Am J Psychiatry 2003; 160: 569–571.

Goldberg TE, Egan MF, Gscheidle T, Coppola R, Weickert T, Kolachana BS, et al. Executive subprocesses in working memory: relationship to catechol-O-methyltransferase Val158Met genotype and schizophrenia. Arch Gen Psychiatry 2003; 60: 889–96.

Gurtin, ME. An introduction to continuum mechanics. Boston: Academic Press; 1987.

Harrison PJ, Weinberger DR. Schizophrenia genes, gene expression, and neuropathology: on the matter of their convergence. Mol Psychiatry 2005; 10: 40–68.

Hashimoto R, Yoshida M, Ozaki N, Yamanouchi Y, Iwata N, Suzuki T, et al. Association analysis of the -308G>A promoter polymorphism of the tumor necrosis factor alpha (TNF-alpha) gene in Japanese patients with schizophrenia. J Neural Transm 2004; 111: 217–21.

Hashimoto R, Yoshida M, Kunugi H, Ozaki N, Yamanouchi Y, Iwata N, et al. A missense polymorphism (H204R) of a Rho GTPase-activating protein, the chimerin 2 gene, is associated with schizophrenia in men. Schizophr Res 2005; 73: 383–5.

Ho BC, Andreasen NC, Nopoulos P, Arndt S, Magnotta V, Flaum M. Progressive structural brain abnormalities and their relationship to clinical outcome: a longitudinal magnetic resonance imaging study early in schizophrenia. Arch Gen Psychiatry 2003; 60: 585–94.

Ho BC, Wassink TH, O'leary DS, Sheffield VC, Andreasen NC. Catechol-O-methyl transferase Val(158)Met gene polymorphism in schizophrenia: working memory, frontal lobe MRI morphology and frontal cerebral blood flow. Mol Psychiatry 2005; 10: 287–98.

Kendler KS. Overview: a current perspective on twin studies of schizophrenia. Am J Psychiatry 1983; 140: 1413–25.

Kondo H, Osaka N, Osaka M. Cooperation of the anterior cingulate cortex and dorsolateral prefrontal cortex for attention shifting. Neuroimage 2004; 23: 670–9.

Kunugi H, Vallada HP, Sham PC, Hoda F, Arranz MJ, Li T, et al. Catechol-O-methyltransferase polymorphisms and schizophrenia: a transmission disequilibrium study in multiply affected families. Psychiatr Genet 1997; 7: 97–101.

Lieberman JA, Tollefson GD, Charles C, Zipursky R, Sharma T, Kahn RS, et al. Antipsychotic drug effects on brain morphology in first-episode psychosis. Arch Gen Psychiatry 2005; 62: 361–70.

Maldjian JA, Laurienti PJ, Kraft RA, Burdette JH. An automated method for neuroanatomic and cytoarchitectonic atlas-based interrogation of fMRI data sets. Neuroimage 2003; 19: 1233–9.

McGue M, Gottesman II, Rao DC. The transmission of schizophrenia under a multifactorial threshold model. Am J Hum Genet 1983; 35: 1161–78.

Nelson KB, Lynch JK. Stroke in newborn infants. Lancet Neurol 2004; 3: 150–8.

Norton N, Kirov G, Zammit S, Jones G, Jones S, Owen R, et al. Schizophrenia and functional polymorphisms in the MAOA and COMT genes: no evidence for association or epistasis. Am J Med Genet 2002; 114: 491–6.

Ohmori O, Shinkai T, Kojima H, Terao T, Suzuki T, Mita T, et al. Association study of a functional catechol-O-methyltransferase gene polymorphism in Japanese schizophrenics. Neurosci Lett 1998; 243: 109–12.

Okubo Y, Saijo T, Oda K. A review of MRI studies of progressive brain changes in schizophrenia. J Med Dent Sci 2001; 48: 61–7.

Palmatier MA, Kang AM, Kidd KK. Global variation in the frequencies of functionally different catechol-O-methyltransferase alleles. Biol Psychiatry 1999; 46: 557–67.

Paus T. Primate anterior cingulate cortex: where motor control, drive and cognition interface. Nat Rev Neurosci 2001; 2: 417–24.

Pezawas L, Verchinski BA, Mattay VS, Callicott JH, Kolachana BS, Straub RE, et al. The brain-derived neurotrophic factor val66met polymorphism and variation in human cortical morphology. J Neurosci 2004; 24: 10099–102.

Selemon LD. Regionally diverse cortical pathology in schizophrenia: clues to the etiology of the disease. Schizophr Bull 2001; 27: 349–77.

Shenton ME, Dickey CC, Frumin M, McCarley RW. A review of MRI findings in schizophrenia. Schizophr Res 2001; 49: 1–52.

Steel RM, Whalley HC, Miller P, Best JJ, Johnstone EC, Lawrie SM. Structural MRI of the brain in presumed carriers of genes for schizophrenia, their affected and unaffected siblings. J Neurol Neurosurg Psychiatry 2002; 72: 455–8.

Stefanis NC, Van Os J, Avramopoulos D, Smyrnis N, Evdokimidis I, Hantoumi I, et al. Variation in catechol-O-methyltransferase val158 met genotype associated with schizotypy but not cognition: a population study in 543 young men. Biol Psychiatry 2004; 56: 510–5.

Sullivan PF, Kendler KS, Neale MC. Schizophrenia as a complex trait: evidence from a meta-analysis of twin studies. Arch Gen Psychiatry 2003; 60: 1187–92.

Takahashi T, Suzuki M, Hagino H, Zhou SY, Kawasaki Y, Nohara S, et al. Bilateral volume reduction of the insular cortex in patients with schizophrenia: a volumetric MRI study. Psychiatry Res 2004; 132: 187–96.

Talairach J, Tournoux P. A coplanar stereotaxic atlas of a human brain. Three-dimensional proportional system: an approach to cerebral imaging. Stuttgart: Thieme; 1988.

Tunbridge EM, Bannerman DM, Sharp T, Harrison PJ. Catechol-O-methyltransferase inhibition improves set-shifting performance and elevates stimulated dopamine release in the rat prefrontal cortex. J Neurosci 2004; 24: 5331–5.

Weinberger DR, Egan MF, Bertolino A, Callicott JH, Mattay VS, Lipska BK, et al. Prefrontal neurons and the genetics of schizophrenia. Biol Psychiatry 2001; 50: 825–44.

Wright IC, McGuire PK, Poline JB, Travere JM, Murray RM, Frith CD, et al. A voxel-based method for the statistical analysis of gray and white matter density applied to schizophrenia. Neuroimage 1995; 2: 244–52.

Yamasue H, Iwanami A, Hirayasu Y, Yamada H, Abe O, Kuroki N, et al. Localized volume reduction in prefrontal, temporolimbic, and paralimbic regions in schizophrenia: an MRI parcellation study. Psychiatry Res 2004; 131: 195–207.

Journal of Cerebral Blood Flow & Metabolism (2006), 1–7

www.jcbfm.com

Estimation of oxygen metabolism in a rat model of permanent ischemia using positron emission tomography with injectable ^{15}O-O_2

Takashi Temma[1], Yasuhiro Magata[2], Yuji Kuge[1], Sayaka Shimonaka[1], Kohei Sano[1], Yumiko Katada[1], Hidekazu Kawashima[3], Takahiro Mukai[3], Hiroshi Watabe[4], Hidehiro Iida[4] and Hideo Saji[1]

[1]*Department of Patho-Functional Bioanalysis, Graduate School of Pharmaceutical Sciences, Kyoto University, Kyoto, Japan;* [2]*Laboratory of Genome Bio-Photonics, Photon Medical Research Center, Hamamatsu University School of Medicine, Hamamatsu, Japan;* [3]*Department of Nuclear Medicine and Diagnostic Imaging, Graduate School of Medicine, Kyoto University, Kyoto, Japan;* [4]*Department of Investigative Radiology, National Cardiovascular Center Research Institute, Suita, Japan*

The threshold of cerebral blood flow (CBF) into infarction in rats has been indicated to be similar to that in patients. However, CBF does not reflect metabolic function, and so estimations of oxygen metabolism have been required. Here, we estimated changes in oxygen metabolism after occluding the right middle cerebral artery (MCA) in rats using an injectable ^{15}O-O_2 we developed. A decrease in CBF (left: 0.67±0.22 mL/min/g, right: 0.44±0.17 mL/min/g, $P<0.05$) and compensatory increase in the oxygen extraction fraction (OEF) (left: 0.42±0.13, right: 0.50±0.19, $P<0.05$) were observed at 1-h after occlusion. In contrast, a marked decrease in CBF and the cerebral metabolic rate for oxygen and a collapse of the compensatory OEF mechanism were found at 24 h after occlusion. Injectable ^{15}O-O_2 could be used to reliably estimate oxygen metabolism in an infarction rat model with positron emission tomography.
Journal of Cerebral Blood Flow & Metabolism advance online publication, 22 March 2006; doi:10.1038/sj.jcbfm.9600302

Keywords: OEF; oxygen metabolism; permanent ischemia; positron emission tomography; rat

Introduction

Stroke is closely related to alterations in cerebral blood flow (CBF), the cerebral metabolic rate for oxygen ($CMRO_2$), the oxygen extraction fraction (OEF), cerebral blood volume, and so on while some neurodegenerative disorders such as Alzheimer's disease and Parkinson's disease are also reported to induce a change in CBF (Derejko *et al*, 2001; Mori, 2002) because of tissue degradation. Therefore, estimation of these circulatory and metabolic parameters is important for both pathophysiological studies and the development or evaluation of new methods for treating stroke.

Studies on changes in parameters of cerebral circulation after the onset of stroke have been performed in several animal models (Belayev *et al*, 1997; Ginsberg, 2003; Heiss *et al*, 1997, 1994; Pappata *et al*, 1993; Takamatsu *et al*, 2000; Tenjin *et al*, 1992; Young *et al*, 1996; Zhao *et al*, 1997) and patients (Baron, 2001; Heiss *et al*, 2001). In the studies using larger animals, CBF, OEF and $CMRO_2$ were estimated after the onset of ischemia by positron emission tomography (PET) with ^{15}O-H_2O and ^{15}O-O_2 gas and used as predictors for the progression of brain infarction. These reports indicated that areas showing a decrease in CBF and compensatory increase in OEF in the early phase of stroke were vital several hours after the onset. Also, in studies with rats as an animal model of ischemia, CBF was certainly indicated to be a good predictor for infarction in comparison with the results for

Correspondence: Dr Y Magata, Laboratory of Genome Bio-Photonics, Photon Medical Research Center, Hamamatsu University School of Medicine, 1-20-1 Handayama, Hamamatsu 431-3192, Japan.
E-mail: magata@hama-med.ac.jp
This study was partly supported by Mitsubishi Pharma Research Foundation. This work was also supported by Grants-in-Aid for Scientific Research and by the 21st Century Center of Excellence Program at Kyoto University 'Knowledge Information Infrastructure for Genome Science' and at Hamamatsu University School of Medicine 'Medical Photonics' from the Ministry of Education, Culture, Sports, Science and Technology, Japan.
Received 4 October 2005; revised 7 February 2006; accepted 10 February 2006

patients (Belayev *et al*, 1997; Ginsberg, 2003; Zhao *et al*, 1997). However, CBF does not reflect cell energy metabolism and so measurements of oxygen metabolism are required to accurately estimate tissue viability. Additionally, since that there are functional differences between rodents and humans (Walovitch *et al*, 1994), careful evaluation is needed when using rats to investigate the pathophysiology and progression of human stroke. On these bases, we adopted MCA occluded rats, widely used ischemia model (Kuge *et al*, 1995; Longa *et al*, 1989; Minematsu *et al*, 1992), and evaluated the changes in CBF, OEF and $CMRO_2$ after the onset of stroke with PET.

On the other hand we recently developed a method of measuring regional OEF in the rat brain noninvasively using PET (Magata *et al*, 2003). Here, we designed experiments to estimate CBF, OEF and $CMRO_2$ by PET in the early and late phases of a permanent ischemia in rats.

Materials and methods

Animals

Male Sprague–Dawley rats (250 to 310 g) supplied by Japan SLC Co. (Hamamatsu, Japan) were housed for 1 week under a 12-h light/12-h dark cycle and given free access to food and water. The animal experiments in this study were conducted in accordance with institutional guidelines and approved by the Kyoto University Animal Care Committee.

Preparation of ^{15}O-Labeled Compounds

The production of ^{15}O-H_2O and injection of ^{15}O-oxygen (injectable ^{15}O-O_2) were conducted as reported previously (Magata *et al*, 2003). Briefly, ^{15}O-H_2O was synthesized by the reduction of ^{15}O-O_2 with H_2 gas (catalyzed by Pd black at 140°C) and trapped in a saline solution. As for injectable ^{15}O-O_2, part of an infusion line kit (Terumo Corporation, Tokyo, Japan) used as a blood reservoir and an artificial lung 18 cm in length (Senko Medical Instrument Mfg Co. Ltd, Tokyo, Japan) designed for small animals such as rats were connected to a peristaltic pump (EYELA roller pump RP-1000, Tokyo Rikakikai Co. Ltd, Tokyo, Japan) to make a closed system. Then, 18 to 20 mL of blood was collected from several rats and filtered with saline-wetted gauze. The blood was circulated (100 mL/min) in the system and ^{15}O-O_2 gas (4100 to 5100 MBq/min/500 ml) was introduced into the artificial lung to prepare injectable ^{15}O-O_2 (51 to 90 MBq/ml).

Animal Preparation

Rats were divided into two groups. One was for the early phase PET experiment ($n=7$, 1 h after the onset of occlusion) and the other was for the late phase experiment ($n=6$, 24 h after the onset of occlusion). The rats were starved for 6 h before the operation and anesthetized with chloral hydrate (i.p. 400 mg/kg). For the early phase group, anesthesia was sustained throughout the experiment. The left femoral artery in each rat was catheterized using a PE 20 catheter (i.d. 0.5 mm, o.d. 0.8 mm) for blood sampling during PET study. Then, the right middle cerebral artery (MCA) was occluded intraluminally using a nylon 4-0 monofilament (Kuge *et al*, 1995; Longa *et al*, 1989; Minematsu *et al*, 1992). For the late phase group, each rat was aroused from anesthesia after the right MCA occlusion and then anesthetized for the catheterization of the left femoral artery and PET experiments. After the completion of the operation, rats were administered i.v. with 100 IU of heparin. The animal was placed supine in a stereotaxic apparatus, and its head was restrained by mouth and ear bars. After the acquisition of a blank scan for 180 mins, the apparatus was placed in a PET camera (SHR-7700L, Hamamatsu Photonics, Hamamatsu, Japan) (Watanabe *et al*, 1997). The position was standardized with the aid of a laser beam, and the desired cranial position in the camera was oriented. Rectal temperature was maintained at around 37 °C with the aid of heating pads and blood gases were measured using a blood gas analyzer (Rapidlab 348, Chiron Diagnostics Ltd, Essex, England) several times during the experiment. After the PET experiments, 2,3,5-triphenyltetrazolium chloride (TTC) staining was performed in some cases for evaluating the progression of stroke.

Positron Emission Tomography Experiments

A transmission scan was performed for 30 mins for attenuation correction following the blank scan. Then, a dynamic PET scan was performed using ^{15}O-H_2O (i.v., 148 to 185 MBq) to measure CBF values 1 h or 24 h after the initiation of MCA occlusion. A second PET scan was performed with the administration of injectable ^{15}O-O_2 (i.v., 74 to 148 MBq) over a 60-secs period to measure OEF values after the radioactivity of ^{15}O-H_2O had decayed in the body. In both cases, the total scan acquisition period was 120 secs and the scan consisted of 12 × 10-second frames. Arterial blood sampling was performed continuously throughout the PET scans and blood centrifugation was also performed for measuring the plasma concentration of ^{15}O radioactivity. The radioactivity of each sample was measured with an NaI well scintillation counter (Packard AutoGamma 500, Packard Instruments, Meriden, CT, USA) calibrated using a ^{22}Na standard radioactive source.

Data Analysis

Positron emission tomography images were obtained as described previously (Magata *et al*, 2003). The rat brain was visualized in four consecutive coronal slices. Then, two regions of interest (ROIs) in each slice, right and left hemispheres, were visually chosen according to the magnetic resonance images obtained previously in the another study using 1.5T MRI. Activity in ROIs was calibrated using a cross calibration factor calculated in

another phantom study with a 10-cm-diameter hollow phantom.

The CBF value in each ROI was calculated by numerically solving the equation (1) as reported previously (Temma *et al*, 2004).

$$R(t) = fA_W(t) * e^{-(f/P+\lambda)t} \quad (1)$$

where the asterisk denotes the convolution integral and other marks are the tissue concentration of ^{15}O radioactivity ($R(t)$), a typical example of that in the late phase experiment is presented in Figure 1, CBF (f), the arterial concentration of ^{15}O-water radioactivity ($A_W(t)$), partition coefficient of water between the brain and blood ($P = 0.8$) and physical decay constant of ^{15}O (λ).

Then, the OEF value was calculated using the same equation (Eq. 2) as that applied to the bolus inhalation of ^{15}O-O_2 gas method (Mintun *et al*, 1984; Shidahara *et al*, 2002), which could be used with this pharmaceutical as shown previously (Magata *et al*, 2003)

$$R(t) = \mathrm{OEF} f A_O(t) * e^{-(f/P+\lambda)t} + fA_W(t) * e^{-(f/P+\lambda)t} + V_B R(1 - V_V' \mathrm{OEF}) A_O(t) \quad (2)$$

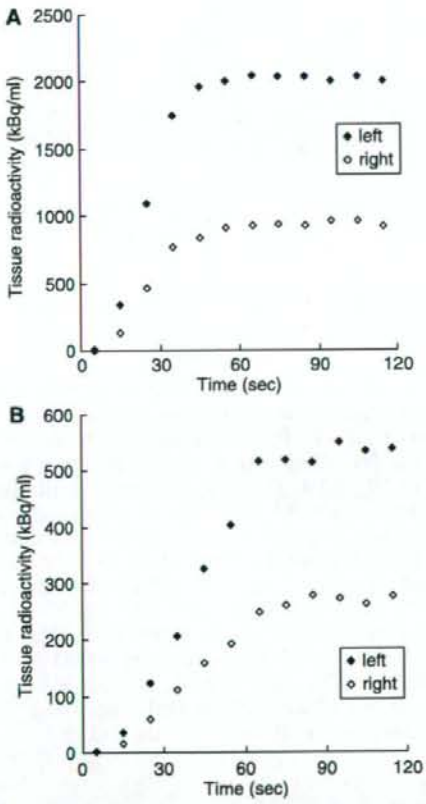

Figure 1 Typical curves of ^{15}O radioactivity obtained by the PET scanning using (**A**) ^{15}O-H_2O and (**B**) injectable ^{15}O-O_2 24 h after the right MCA occlusion.

where the arterial concentration of ^{15}O-O_2 radioactivity ($A_O(t)$), cerebral blood volume ($V_B = 0.04$ mL/g), the hematocrit ratio between central and peripheral regions ($R = 0.85$) and the effective venous ratio in the brain ($V_V' = 0.835$) are used.

The $CMRO_2$ value was calculated using equation (3). In this equation, Hb is gram hemoglobin/mL blood and %Sat is percent saturation of O_2 (Shidahara *et al*, 2002).

$$\mathrm{CMRO_2} = \frac{(1.39 \times \mathrm{Hb} \times \%\mathrm{Sat})}{100} \times \mathrm{OEF} \times \mathrm{CBF} \quad (3)$$

Results

Injectable ^{15}O-O_2 Labeling

The shape of an artificial lung was modified to increase ^{15}O labeling efficiency. Namely, the artificial lung used was three times longer (18 cm) than the previous version while the density of plastic fibers and diameter of the lung were unchanged (Magata *et al*, 2003). In this system, 90 MBq/ml was obtained at maximum.

Physiological Parameters

Blood gases were analyzed several times during the experiment (Table 1). Although several parameters were significantly changed, these changes were slight and levels were not in the abnormal range.

Studies at 1 h After Onset

The relationships between CBF, OEF and $CMRO_2$ at 1 h after the occlusion are shown in scatter diagrams (Figures 2 and 3). As revealed in Figure 2, in the right hemisphere, a decrease in CBF and compensatory increase in OEF were indicated in comparison with the opposite side, inducing a good reciprocal relationship as a whole. Also, the decrease in CBF in the right hemisphere was not so marked. Figure 3 shows the relationship between CBF and $CMRO_2$.

Table 1 Arterial blood gas values before and after PET experiments in MCA occlusion

	1 h		*24 h*	
	Before	*After*	*Before*	*After*
pH	7.32 (0.03)	7.33 (0.03)	7.36 (0.04)	7.35 (0.04)
PO_2 (mm Hg)	97.4 (5.7)	102.8 (10)	94.8 (7.4)	101.5 (4.3)*
PCO_2 (mm Hg)	44.3 (4.2)	39.8 (3.4)	39.7 (4.8)	36.9 (3.7)*
Hct (%)	54.4 (4.8)	51.5 (3.8)*	55 (3.3)	53.5 (3.1)
O_2Sat (%)	96.9 (0.4)	97.2 (0.8)	96.9 (0.7)	97.4 (0.3)*
Hb (g/dl)	18.5 (1.6)	17.5 (1.3)*	18.7 (1.2)	18.2 (1.0)

Statistical differences in each physiological parameter between before and after PET experiments were determined using the Wilcoxon signed-rank test; *$P < 0.05$.
Values listed are means (s.d.).

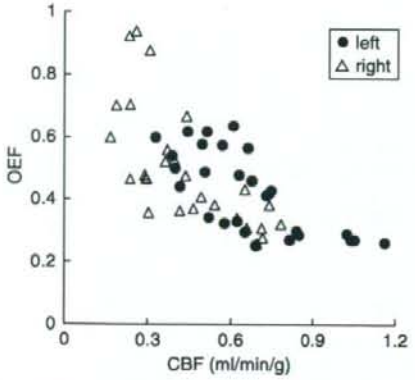

Figure 2 Scatter diagram of CBF (mL/min/g) and OEF values 1 h after the onset of MCA occlusion.

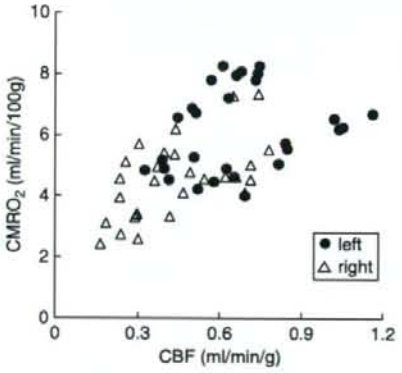

Figure 3 Scatter diagram of CBF (mL/min/g) and $CMRO_2$ (mL/min/100 g) values 1 h after the onset of MCA occlusion.

These two values also exhibit a good correlation, in which the decrease in $CMRO_2$ in the right hemisphere was not so marked.

Studies at 24 h After Onset

The relationships among parameters at 24 h after the occlusion are shown in scatter diagrams (Figures 4 and 5). As shown in Figure 4, in the right hemisphere, the decrease in CBF was more pronounced than at 1 h (Figure 2) and there was no compensatory increase in OEF, resulting in a loss of the good correlation between CBF and OEF. Figure 5 shows the relationship between CBF and $CMRO_2$. The right hemisphere exhibited a marked decrease in $CMRO_2$.

Quantitative Values of Cerebral Blood Flow, Oxygen Extraction Fraction and Cerebral Metabolic Rate for Oxygen

Figure 6 and Table 2 show the averaged hemispheric values of CBF, OEF and $CMRO_2$ at 1 h ($n=7$) and

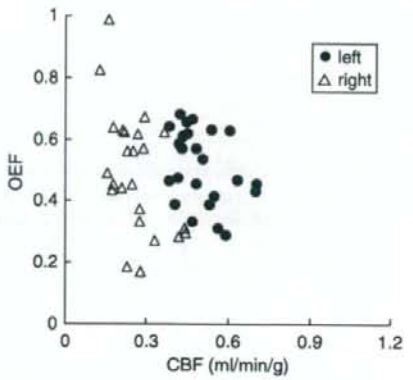

Figure 4 Scatter diagram of CBF (mL/min/g) and OEF values 24 h after the onset of MCA occlusion.

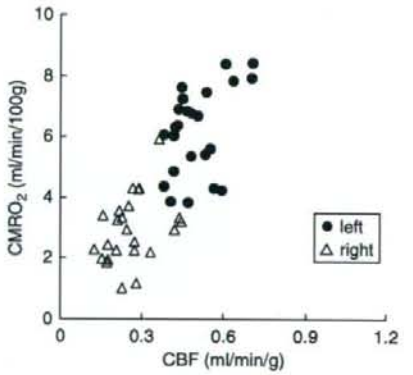

Figure 5 Scatter diagram of CBF (mL/min/g) and $CMRO_2$ (mL/min/100 g) values 24 h after the onset of MCA occlusion.

24 h ($n=6$) after the onset of MCA occlusion. In the right hemisphere at 1 h, the decrease in CBF was not so marked (0.44 ± 0.17 mL/min/g; $P<0.05$ compared with the left side) and a compensatory increase in OEF (0.50 ± 0.19; $P<0.05$ compared with the left side) was observed, inducing a slight decrease in $CMRO_2$ (4.5 ± 1.1 mL/min/100 g; $P<0.05$ compared with the left side). In contrast, at 24 h, there was a marked decrease in CBF (0.26 ± 0.07 mL/min/g, $P<0.05$ compared with both the left side and at 1 h) and no compensatory increase in OEF (0.49 ± 0.19; OEF in the left hemisphere was 0.51 ± 0.12, not significant with each other), resulting in a large decrease in $CMRO_2$ (2.9 ± 0.8 mL/min/100 g; $P<0.05$ compared with both the left side and at 1 h).

Discussion

In our previous report (Magata *et al*, 2003), up to 72 MBq/ml of injectable ^{15}O-O_2 was obtained with

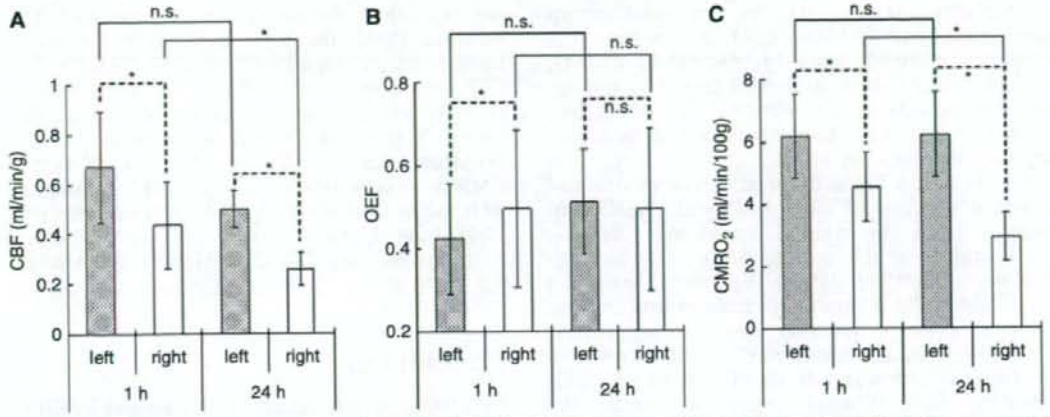

Figure 6 The averaged hemispheric values of (**A**) CBF (mL/min/g), (**B**) OEF and (**C**) $CMRO_2$ (mL/min/100 g) obtained by PET 1 ($n = 7$) and 24 h ($n = 6$) after the onset of MCA occlusion. Significant differences in each parameter (CBF, OEF, $CMRO_2$) between the left and right hemispheres at the same time point and between 1 h and 24 h on the same hemisphere were determined using the Wilcoxon signed-rank test and the Mann–Whitney *U*-test, respectively; $^*P < 0.05$, n.s. not significant.

Table 2 The averaged hemispheric values of CBF (mL/min/g), OEF and $CMRO_2$ (mL/min/100 g) obtained by PET 1 (n = 7) and 24 hours (n = 6) after the onset of MCA occlusion.

	1 h		*24 h*	
	Left	*Right*	*Left*	*Right*
CBF (mL/min/g)	0.67 (0.22)	0.44 (0.17)*	0.50 (0.08)	0.26 (0.07)*,†
OEF	0.42 (0.13)	0.50 (0.19)*	0.51 (0.12)	0.49 (0.19)
$CMRO_2$ (mL/min/100 g)	6.2 (1.3)	4.5 (1.1)*	6.2 (1.4)	2.9 (0.8)*,†

Significant differences in each parameter (CBF, OEF, $CMRO_2$) between the left and right hemispheres at the same time point and between 1 and 24 h on the same hemisphere were determined using the Wilcoxon signed-rank test ($^*P < 0.05$) and the Mann–Whitney *U*-test ($^†P < 0.05$), respectively. Values listed are means (s.d.).

an artificial lung (6 cm length) and about 10 ml of blood. In the present study, the artificial lung was made three times longer to increase the labeling efficiency. First, we used three small artificial lungs connected in series to improve the labeling efficiency. In that system, more blood was needed for summation of the dead volume of each lung, and, the labeling efficiency, radioactivity per unit blood volume, did not increase. Since the total activity in the labeling system is constant if the radioactivity in the supplied gas is constant, highly specific activity of injectable ^{15}O-O_2 can be obtained when a small amount of blood is used. Therefore, the 'long' artificial lung can increase the specific activity of injectable ^{15}O-O_2 owing to the small dead volume. Actually, with this new artificial lung and 18.6 ml of blood, 90 MBq/ml of injectable ^{15}O-O_2 was obtained.

During the experiments, arterial blood gases were analyzed several times (Table 1). At both 1 and 24 h, significant changes were observed in two or three parameters. At 1 h, Hct and Hb decreased after the experiment, indicating slight hemolytic anemia. At 24 h, pO_2, pCO_2 and O_2Sat changed during the PET scans. These values, especially pCO_2, are known to be closely related to the depth of anesthesia and so might reflect a change in the condition of the animal in PET studies. In any case, the changes of these parameters were not so marked and they might not affect the results of experiments.

At 1 h after the onset of MCA occlusion, CBF decreased slightly but significantly in the right hemisphere in comparison with the left side; some ROIs showed normal values and others showed low values (Figure 2). The OEF increased in ROIs with decreased CBF, but not in ROIs with normal CBF (Figure 2). The results indicate that the metabolic compensatory mechanism worked well at 1 h after MCAO. Cerebral metabolic rate for oxygen was also kept in the area of low CBF (Figure 3), and a good correlation between CBF and $CMRO_2$ with a gentle slope was obtained (Figure 3), suggesting that the compensatory mechanism was working well at this time point.

At 24 h after the onset of MCA occlusion, while all ROIs in the right hemisphere showed severely decreased CBF with small variation, OEF showed a

large variation (Figure 4). In the relationship between CBF and $CMRO_2$, all ROIs in the right hemisphere showed severely decreased $CMRO_2$ (Figure 5). These results indicated that the compensatory mechanism at 1 h after MCAO onset had collapsed at 24 h and the progression of ischemic injury was severer than at 1 h.

In Figure 6 and Table 2, quantitative values and standard deviations of CBF, OEF and $CMRO_2$ are summarized. In the right hemisphere, CBF decreased slightly at 1 h and severely at 24 h. Both values were significantly low compared with the opposite sides ($P<0.05$) at both time points and the difference between the 24 h was also significant ($P<0.05$). In the left hemisphere, CBF showed a little decrease but was not significant during 24 h ($P=0.0865$). Since $CMRO_2$ expressed exactly the same values at both time points, the decrease in CBF might not mean a metabolic dysfunction but a vascular disturbance at 24 h. Although blood vessels in the left hemisphere should not be affected directly in our MCAO operation, the progression of the ischemic damage in the right hemisphere included both the spreading of the ischemic core and the disturbance of surrounding blood vessels so that it is considered that the decrease in CBF on the opposite side could have occurred. Furthermore, $CMRO_2$ in the left hemisphere was close to the value obtained previously in normal rats using ^{133}Xe as a CBF tracer and a surgical method for determining OEF (6.3 ± 0.3 mL/min/100 g) (Kozniewska and Szczepanska-Sadowska, 1990). It underlined the preceding discussion that the brain tissue in the left hemisphere was not damaged at all during 24 h and the reason for the little decrease in CBF was vascular disturbance.

In the right hemisphere, $CMRO_2$ decreased severely during 24 h in the same manner as CBF (Figure 6, Table 2). Since these values did not represent $CMRO_2$ in the ischemic core but just values in the entire right hemisphere because of the large size of ROIs, it is difficult to discuss the progression of impairment. However, taken together with the decreases in CBF in both hemispheres during 24 h, the decrease in $CMRO_2$ might not mean an ischemic core-specific progression of tissue disturbance but a spreading of the ischemic damage throughout the hemisphere. In fact, TTC staining revealed no sign of disturbance at 1 h but severe disruption at 24 h in the right hemisphere.

Meanwhile, an obvious change of OEF was also evident during 24 h (Figure 6, Table 2). The increase in OEF in the right hemisphere compared with the left side at 1 h after the onset of MCAO ($P<0.05$) showed that the metabolic compensatory mechanism was working well. However, at 24 h, the OEF was the same in both hemispheres ($P=0.7532$), which indicates that the compensatory mechanism did not function at 24 h after the onset. Therefore, considering that the condition in the left hemisphere at 1 h was actually normal or stage I in the course of the ischemic disorder (Nemoto *et al*, 2004; Powers, 1991), the right hemisphere at 1 h might include partly stage II and stage III (Figures 2 and 3; CBF was normal or decreased, OEF increased and $CMRO_2$ was normal or slightly decreased), the left hemisphere at 24 h might be expressed at stage II (Figures 4 and 5; CBF decreased, OEF increased, $CMRO_2$ was normal) and the right hemisphere at 24 h might include early and severe phases of stage III (Figures 4 and 5; CBF decreased, OEF increased or decreased and $CMRO_2$ strikingly decreased).

Conclusion

In this paper, we estimated the changes in CBF, OEF and $CMRO_2$ after the onset of MCA occlusion in rats by PET using injectable ^{15}O-O_2. In the early phase after occlusion, a decrease in CBF and compensatory increase in OEF were shown, and in contrast, CBF and $CMRO_2$ were severely decreased in the late phase. This is the first report to indicate reliable oxygen metabolism in a MCAO rat model using PET.

References

Baron JC (2001) Perfusion thresholds in human cerebral ischemia: historical perspective and therapeutic implications. *Cerebrovasc Dis* 11(Suppl 1):2–8

Belayev L, Zhao W, Busto R, Ginsberg MD (1997) Transient middle cerebral artery occlusion by intraluminal suture: I. Three-dimensional autoradiographic image-analysis of local cerebral glucose metabolism–blood flow interrelationships during ischemia and early recirculation. *J Cereb Blood Flow Metab* 17:1266–80

Derejko M, Slawek J, Lass P, Nyka WM (2001) Cerebral blood flow changes in Parkinson's disease associated with dementia. *Nucl Med Rev Cent East Eur* 4:123–7

Ginsberg MD (2003) Adventures in the pathophysiology of brain ischemia: penumbra, gene expression, neuroprotection: the 2002 Thomas Willis Lecture. *Stroke* 34:214–23

Heiss WD, Graf R, Lottgen J, Ohta K, Fujita T, Wagner R *et al* (1997) Repeat positron emission tomographic studies in transient middle cerebral artery occlusion in cats: residual perfusion and efficacy of postischemic reperfusion. *J Cereb Blood Flow Metab* 17:388–400

Heiss WD, Graf R, Wienhard K, Lottgen J, Saito R, Fujita T *et al* (1994) Dynamic penumbra demonstrated by sequential multitracer PET after middle cerebral artery occlusion in cats. *J Cereb Blood Flow Metab* 14:892–902

Heiss WD, Kracht LW, Thiel A, Grond M, Pawlik G (2001) Penumbral probability thresholds of cortical flumazenil binding and blood flow predicting tissue outcome in patients with cerebral ischaemia. *Brain* 124:20–9

Kozniewska E, Szczepanska-Sadowska E (1990) V2-like receptors mediate cerebral blood flow increase following vasopressin administration in rats. *J Cardiovasc Pharmacol* 15:579–85

Kuge Y, Minematsu K, Yamaguchi T, Miyake Y (1995) Nylon monofilament for intraluminal middle cerebral artery occlusion in rats. *Stroke* 26:1655–8

Longa EZ, Weinstein PR, Carlson S, Cummins R (1989) Reversible middle cerebral artery occlusion without craniectomy in rats. *Stroke* 20:84–91

Magata Y, Temma T, Iida H, Ogawa M, Mukai T, Iida Y *et al* (2003) Development of injectable O-15 oxygen and estimation of rat OEF. *J Cereb Blood Flow Metab* 23: 671–6

Minematsu K, Li L, Fisher M, Sotak CH, Davis MA, Fiandaca MS (1992) Diffusion-weighted magnetic resonance imaging: rapid and quantitative detection of focal brain ischemia. *Neurology* 42:235–40

Mintun MA, Raichle ME, Martin WR, Herscovitch P (1984) Brain oxygen utilization measured with O-15 radiotracers and positron emission tomography. *J Nucl Med* 25:177–87

Mori S (2002) Responses to donepezil in Alzheimer's disease and Parkinson's disease. *Ann NY Acad Sci* 977: 493–500

Nemoto EM, Yonas H, Kuwabara H, Pindzola RR, Sashin D, Meltzer CC *et al* (2004) Identification of hemodynamic compromise by cerebrovascular reserve and oxygen extraction fraction in occlusive vascular disease. *J Cereb Blood Flow Metab* 24:1081–9

Pappata S, Fiorelli M, Rommel T, Hartmann A, Dettmers C, Yamaguchi T *et al* (1993) PET study of changes in local brain hemodynamics and oxygen metabolism after unilateral middle cerebral artery occlusion in baboons. *J Cereb Blood Flow Metab* 13: 416–24

Powers WJ (1991) Cerebral hemodynamics in ischemic cerebrovascular disease. *Ann Neurol* 29:231–40

Shidahara M, Watabe H, Kim KM, Oka H, Sago M, Hayashi T *et al* (2002) Evaluation of a commercial PET tomograph-based system for the quantitative assessment of rCBF, rOEF and $rCMRO_2$ by using sequential administration of ^{15}O-labeled compounds. *Ann Nucl Med* 16:317–27

Takamatsu H, Tsukada H, Kakiuchi T, Nishiyama S, Noda A, Umemura K (2000) Detection of reperfusion injury using PET in a monkey model of cerebral ischemia. *J Nucl Med* 41:1409–16

Temma T, Magata Y, Mukai T, Kitano H, Konishi J, Saji H (2004) Availability of *N*-isopropyl-p-[(125)I]iodoamphetamine (IMP) as a practical cerebral blood flow (CBF) indicator in rats. *Nucl Med Biol* 31:811–4

Tenjin H, Ueda S, Mizukawa N, Imahori Y, Hino A, Ohmori Y *et al* (1992) Positron emission tomographic measurement of acute hemodynamic changes in primate middle cerebral artery occlusion. *Neurol Med Chir (Tokyo)* 32:805–10

Walovitch RC, Cheesman EH, Maheu LJ, Hall KM (1994) Studies of the retention mechanism of the brain perfusion imaging agent 99mTc-bicisate (99mTc-ECD). *J Cereb Blood Flow Metab* 14(Suppl 1):S4–11

Watanabe M, Okada H, Shimizu K, Omura T, Yoshikawa E, Kosugi T *et al* (1997) A high resolution animal PET scanner using compact PS-PMT detectors. *IEEE Trans Nucl Sci* 44:1277–82

Young AR, Sette G, Touzani O, Rioux P, Derlon JM, MacKenzie ET *et al* (1996) Relationships between high oxygen extraction fraction in the acute stage and final infarction in reversible middle cerebral artery occlusion: an investigation in anesthetized baboons with positron emission tomography. *J Cereb Blood Flow Metab* 16:1176–88

Zhao W, Belayev L, Ginsberg MD (1997) Transient middle cerebral artery occlusion by intraluminal suture: II. Neurological deficits, and pixel-based correlation of histopathology with local blood flow and glucose utilization. *J Cereb Blood Flow Metab* 17:1281–90

Widespread Decrease of Nicotinic Acetylcholine Receptors in Parkinson's Disease

Masahiro Fujita, MD, PhD,[1] Masanori Ichise, MD,[1] Sami S. Zoghbi, PhD,[1] Jeih-San Liow, PhD,[1] Subroto Ghose, MD, PhD,[1] Douglass C. Vines, BS,[1] Janet Sangare, C-RNP, MS,[1] Jian-Qiang Lu, MD, PhD,[1] Vanessa L. Cropley, BS,[1] Hidehiro Iida, PhD,[2] Kyeong Min Kim, PhD,[2] Robert M. Cohen, PhD, MD,[3] William Bara-Jimenez, MD,[4] Bernard Ravina, MD,[5] and Robert B. Innis, MD, PhD[1]

Objective: **Nicotinic acetylcholine receptors have close interactions with the dopaminergic system and play critical roles in cognitive function. The purpose of this study was to compare these receptors between living PD patients and healthy subjects.** ***Methods:*** **Nicotinic acetylcholine receptors were imaged in 10 nondemented Parkinson's disease patients and 15 age-matched healthy subjects using a single-photon emission computed tomography ligand [^{123}I]5-iodo-3-[2(*S*)-2-azetidinylmethoxy]pyridine. Using an arterial input function, we measured the total distribution volume (V_T specific plus nondisplaceable), as well as the delivery (K_1).** ***Results:*** **Parkinson's disease showed a widespread significant decrease (approximately 10%) of V_T in both cortical and subcortical regions without a significant change in K_1.** ***Interpretation:*** **These results indicate the importance of extending the study to demented patients.**

Ann Neurol 2006;59:174–177

In addition to the well-documented loss of dopaminergic neurons, a number of animal and clinical studies have shown that nicotinic acetylcholine receptors (nAChRs) play critical roles in Parkinson's disease (PD). nAChR activation stimulates dopamine release in the striatum,[1] and an agonist at nAChRs showed synergistic therapeutic effects with L-dopa in a monkey model of PD.[2] Epidemiological studies showed that cigarette smoking protects against PD.[3] Both animal and human studies have shown that nAChR is one of the central components in cognitive function,[4] and a substantial number of PD patients become demented. Finally, most postmortem studies showed widespread decrease of nAChRs both in striatum and cerebral cortices of PD patients.[5–8] However, as in most other postmortem studies, many of these lacked critical clinical information such as the presence of dementia and a history of cigarette smoking. Therefore, it is critical to image nAChRs in living PD patients whose clinical information is available to study changes and to explore possible therapeutic intervention at these receptors. However, to our knowledge, such a study has not been published.

Recently, 3-[2(*S*)-2-azetidinylmethoxy]pyridine (A-85380) has been developed,[9] which has high affinity to the predominant type of nAChRs in the brain composed of α_4 and β_2 subunits.[10] A few analogs of A-85380, including [^{123}I]5-iodo-3-[2(*S*)-2-azetidinylmethoxy]pyridine (5-I-A-85380), have been radiolabeled and used successfully in humans.[11,12] An ex vivo study in nonhuman primate has shown that radiolabeled metabolites of [^{123}I] 5-I-A-85380 do not cross the blood–brain barrier.[13] 5-I-A-85380 labels several β_2-containing nAChRs, including $\alpha_4\beta_2$- (the most predominant nicotinic receptor in human brain), $\alpha_3\beta_2$-, and $\alpha6\beta2$-containing subtypes.[14]

The purpose of this study was to perform a pilot study of nAChR imaging using [^{123}I]5-I-A-85380 in early to moderate stage PD patients.

Subjects and Methods

Subjects

The study was approved by National Institute of Neurological Disorders and Stroke and National Institute of Mental Health institutional review boards. Patients were recruited from National Institute of Neurological Disorders and Stroke clinics. Control subjects were healthy volunteers recruited from community via advertisement who did not have a history or signs of neurological disorders. After complete description of the study to the subjects, written informed consent was obtained. Sample demographics and clinical characteristics are shown in Table 1. For all participants, the absence of axial focal lesions was confirmed by a neuroradiologist using noncontrast magnetic resonance imaging. All patients and healthy subjects had not smoked cigarettes for at least 5 years. None of the patients had used cholinergic or anticholinergic medications within 60 days of the single-photon emission computed tomography (SPECT) scan. On the day of the SPECT scans, all patients continued dopaminergic medications including carbidopa/L-dopa. There was no significant difference in age between PD patients and healthy subjects.

From the [1]Molecular Imaging Branch, National Institute of Mental Health, National Institutes of Health, Bethesda, MD; [2]Investigative Radiology, National Cardiovascular Center Research Institute, Suita, Osaka, Japan; [3]Geriatric Psychiatry Branch, National Institute of Mental Health; [4]Experimental Therapeutics Branch, National Institute of Neurological Disorders and Stroke; and [5]Clinical Trials, Extramural Research, National Institute of Neurological Disorders and Stroke, National Institutes of Health, Bethesda, MD.

Received May 15, 2005, and in revised form Jun 24. Accepted for publication Jun 30, 2005.

Published online Dec 27, 2005 in Wiley InterScience (www.interscience.wiley.com). DOI: 10.1002/ana.20688

Address correspondence to Dr Fujita, Molecular Imaging Branch, National Institute of Mental Health, Building 1, Room B3-10, 1 Center Drive, MSC-0135, Bethesda, MD. E-mail: fujitam@intra.nimh.nih.gov

Table 1. Sample Demographics and Clinical Characteristics

Characteristics	Healthy	PD
N	15	10
Mean age (±SD), yr	59 ± 5	56 ± 3
Sex, F/M	10/5	4/6
Cigarette smoking	No	No
Cholinergic medication	No	No
Dopaminergic medication	No	Yes
Mean [^{123}I]5-I-A-85380 dose (±SD), MBq	486 ± 79	506 ± 75
Mean Hoehn and Yahr staging (±SD)		2.5 ± 0.4
Mean total Unified Parkinson's Disease Rating Scale score (±SD)		46 ± 5[a]
Mean Mini-Mental Status Examination score		≥27
Mean Mattis Dementia Rating Scale score (±SD)		135 ± 4[b]

[a]N = 9; [b]N = 8.

PD = Parkinson's disease; SD = standard deviation.

Clinical Ratings

Motor function was evaluated by Unified Parkinson's Disease Rating Scale and Hoehn and Yahr staging. Cognitive function was measured with Mini-Mental Status Examination and Mattis Dementia Rating Scale.

Single-Photon Emission Computed Tomography

[^{123}I]5-I-A-85380 was prepared as described previously.[12] SPECT data were acquired using a triple-headed camera with low-energy, high-resolution, parallel hole collimators (Trionix XLT-20; Triad, Twinsburg, OH). Initially, a transmission scan was obtained using a ^{153}Gd line source. Subsequently, [^{123}I]5-I-A-85380 was administered intravenously as a bolus (injection dose: healthy, 486 ± 79MBq; PD, 506 ± 75MBq; no significant difference, with these and subsequent data expressed as mean ± standard deviation). SPECT data were acquired at 0 to 40, 115 to 135, and 210 to 230 minutes. Arterial samples were obtained every 15 seconds for the first 2 minutes and at 3, 4, 5, 10, 30, 80, 120, and 180 minutes.

Plasma Analysis

Plasma [^{123}I]5-I-A-85380 concentration and the free fraction (f_1) were determined as described previously.[12]

Image Analysis

SPECT projection data were reconstructed on a 64 × 64 matrix with pixel size of 4.48 × 4.48 × 4.48mm in the *x*-, *y*-, and *z*-axis, respectively, with correction for attenuation and scattered radiation.[15] Parametric images of the delivery of the radioligand (K_1) and total distribution volume (V) were created using a multilinear algorithm[16,17] implemented in PMOD 2.55 (http://www.pmod.com/technologies/index.html). Plasma free [^{123}I]5-I-A-85380 levels were used to calculate V instead of using plasma total (free plus protein bound) [^{123}I]5-I-A-85380 because patients were taking medication and concomitant medication might change plasma protein binding of [^{123}I]5-I-A-85380. Parametric images were spatially normalized to a standard anatomic orientation (Montreal Neurological Institute space) based on K_1 images and using Statistical Parametric Mapping version '02 (SPM2; http://www.fil.ion.ucl.ac.uk/spm). Spatially normalized K_1 and V images were smoothed with 10mm full-width at half-maximum. To confirm the magnitude of changes in V, we obtained volume of interest data from brain regions in Montreal Neurological Institute space listed on Table 2.

Statistical Analysis

SPM2[18] was used for statistical analysis. Two-sample t test was applied to compare K_1 and V between patients and healthy subjects, and simple regression analysis was applied to study the relationship between V and clinical ratings. Gray matter threshold was set at 20% for V and 80% for K_1 images, respectively. Because each pixel had a measured value of K_1 or V, global normalization was not applied. No sphericity correction was applied by assuming replication over groups. False-discovery rate of p less than 0.05 and cluster-level corrected p less than 0.05 were considered significant.

A two-sample t test was applied to compare plasma free fraction of [^{123}I]5-I-A-85380 between groups.

Results

Patients were in the early to moderate stages of PD and were not demented (see Table 1). Patients tended to show lower f_1 values than healthy subjects ($p = 0.09$; see Table 2).

An SPM t test showed a significant decrease of V in many brain regions with the greatest T value of 4.96 (Fig). The decrease measured by the volume of interest was 15% in thalamus, whereas occipital and frontal cortices showed only 3 and 5% decreases, respectively, where many voxels did not reach significance. Decreases in parietal and temporal cortices were 8 to 9% (see Table 2). SPM did not detect a significant increase of V in any brain region in patients. There was neither a significant increase nor a decrease of K_1 in any re-

Table 2. Plasma-Free Fraction and Total Distribution Volume of [^{123}I]5-I-A-85380

Measurements	Healthy	PD
Plasma-free fraction, %	48.1 ± 4.4	45.3 ± 3.1
Total distribution volume, ml/cm^3		
Thalamus	71.9 ± 13.5	61.2 ± 10.7
Caudate	41.9 ± 6.2	36.9 ± 4.3
Putamen	44.4 ± 6.7	40.2 ± 5.6
Pons	43.3 ± 8.1	39.0 ± 8.1
Frontal cortex	24.9 ± 3.1	23.7 ± 3.1
Parietal cortex	26.9 ± 3.5	24.4 ± 3.0
Temporal cortex	30.7 ± 3.9	28.1 ± 4.0
Occipital cortex	27.1 ± 3.6	26.3 ± 4.2
Cerebellum	33.8 ± 6.2	29.2 ± 5.9[a]

[a]One patient was excluded whose cerebellum was partially out of field of view.

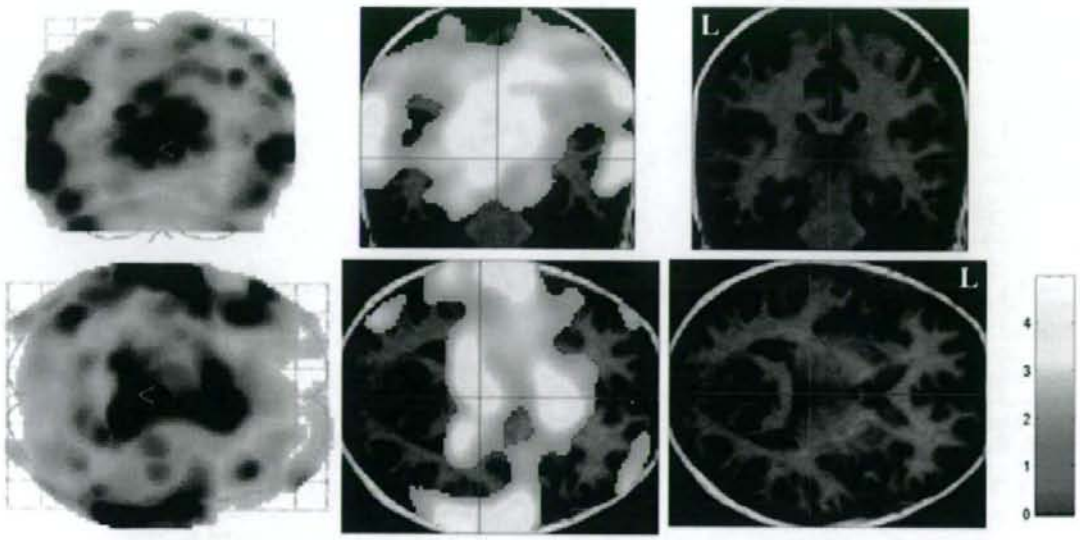

Fig. Brain areas with a significant decrease of [^{123}I]5-I-A-85380 distribution volume (V) *in Parkinson's disease patients detected with a two-sample* t *test in Statistical Parametric Mapping version '02. Areas with a significant decrease are displayed in the glass brain (left) and on transverse and coronal slices through thalamus of a magnetic resonance (MR) image of a control subject (middle). Corresponding MR images without superimposition are shown on the right. Highlighted areas showed* p *less than 0.05 false-discovery rate, which was corrected for multiple comparisons. The area also showed cluster-level corrected* p *less than 0.001. Color bar shows* T *values with the maximum value of 4.96. Note that the glass brain view displays decreases in the entire brain superimposed to anteroposterior (top left) or top-bottom (bottom left) views, whereas the MR images with the superimposition display decreases on single slices.*

gion. There was no significant regression between any clinical rating scores and *V*.

Discussion

In this study, we detected a significant and widespread decrease of nAChRs in early to moderately affected, nondemented PD patients by applying accurate quantification with the measurement of arterial input function and the plasma free fraction (f_1) of [^{123}I]5-I-A-85380 in each subject. Such measurements made the outcome of imaging studies free from intersubject and between-group differences in the metabolism and the protein binding of the imaging agent. Because patients tended to show lower f_1 values, if total plasma parent had been used instead of free [^{123}I]5-I-A-85380, the decrease in *V* would have been overestimated. Furthermore, for accurate measurement, scatter correction[15] and a pixel-based modeling that minimizes noise-induced biases[16,17] were applied.

There are three possible reasons that the decreases in *V* detected in this study were smaller than those reported at postmortem (>30% in most studies). First, because there is no large region devoid of nAChRs, it was not possible to measure nondisplaceable radioactivity, which then could have been used to calculate specific binding of [^{123}I]5-I-A-85380. Because *V* is a summation of specific and nondisplaceable distribution volumes, a decrease of specific binding was underestimated. Second, in this pilot study, only nondemented PD patients were enrolled, whereas postmortem studies found larger decreases in nAChRs in demented patients.[5,7] Therefore, postmortem studies including demented patients showed greater decreases in nAChR than in this study. The lack of significant regression between clinical ratings and *V* may also be explained by a fairly uniform population of nondemented patients. Third, whereas B_{max} is measured in postmortem studies, B_{max}/K_d plus nondisplaceable activity is measured by *in vivo* imaging studies including this one. If there were a decrease in K_d measured *in vivo* in addition to a decrease in B_{max}, a decrease in B_{max}/K_d would not be as great as that in B_{max}. In fact, a postmortem study reported a nonsignificant but substantial 10 to 40% decrease in K_d in both cortical and subcortical regions.[6]

There are a couple of factors that may confound interpretation of the results of this study. All patients were taking L-dopa–containing medications. L-Dopa treatment significantly decreased *in vitro* [^{125}I]5-I-A-85380 binding in the striatum, but not in cerebral cortex in normal squirrel monkeys.[19] However, in the same study, L-dopa treatment did not decrease [^{125}I]5-I-A-85380

binding in the same regions in 1-methyl-4-phenyl-1,2,3,6-tetrahydropyridine–treated animals whose dopaminergic terminals were almost completely destroyed. Therefore, the widespread decreases in nAChRs found in this study are more likely to be the result of PD pathology than L-dopa treatment. Brain atrophy can cause widespread decrease in nAChRs detected in SPECT. However, a voxel-based morphometric study on nondemented patients did not detect a widespread decrease in gray matter volume.[20] By taking together the factors described earlier, nondemented patients with PD did show a widespread decrease of B_{max}/K_d in β_2-containing nAChRs both in cortices and subcortical regions. Because postmortem studies have shown greater decreases in nAChRs in demented patients, it would be interesting to extend the study to include such patients.

This study was supported by the NIH (Intramural Program, 2D1MH002796-04, R.B.I.).

We thank Dr C. Chen and the National Institutes of Health Nuclear Medicine Department for providing the SPECT camera for this study; Drs C. Burger, P. Rudnicki, K. Mikolajczyk, M. Grodzki, and M. Szabatin for providing PMOD 2.55; and A. Crawley, J. Szczepanik, and M. Gillespie for subject recruitment.

References

1. Rapier C, Lunt GG, Wonnacott S. Stereoselective nicotine-induced release of dopamine from striatal synaptosomes: concentration dependence and repetitive stimulation. J Neurochem 1988;50:1123–1130.
2. Schneider JS, Pope-Coleman A, Van Velson M, et al. Effects of SIB-1508Y, a novel neuronal nicotinic acetylcholine receptor agonist, on motor behavior in parkinsonian monkeys. Mov Disord 1998;13:637–642.
3. Tanner CM, Goldman SM, Aston DA, et al. Smoking and Parkinson's disease in twins. Neurology 2002;58:581–588.
4. Picciotto MR, Zoli M. Nicotinic receptors in aging and dementia. J Neurobiol 2002;53:641–655.
5. Rinne JO, Myllykyla T, Lonnberg P, Marjamaki P. A postmortem study of brain nicotinic receptors in Parkinson's and Alzheimer's disease. Brain Res 1991;547:167–170.
6. Aubert I, Araujo DM, Cecyre D, et al. Comparative alterations of nicotinic and muscarinic binding sites in Alzheimer's and Parkinson's diseases. J Neurochem 1992;58:529–541.
7. Lange KW, Wells FR, Jenner P, Marsden CD. Altered muscarinic and nicotinic receptor densities in cortical and subcortical brain regions in Parkinson's disease. J Neurochem 1993;60: 197–203.
8. Quik M, Bordia T, Forno L, McIntosh JM. Loss of alphaconotoxinMII- and A85380-sensitive nicotinic receptors in Parkinson's disease striatum. J Neurochem 2004;88:668–679.
9. Abreo MA, Lin NH, Garvey DS, et al. Novel 3-pyridyl ethers with subnanomolar affinity for central neuronal nicotinic acetylcholine receptors. J Med Chem 1996;39:817–825.
10. Mukhin AG, Gundisch D, Horti AG, et al. 5-Iodo-A-85380, an a4b2 subtype-selective ligand for nicotinic acetylcholine receptors. Mol Pharmacol 2000;57:642–649.
11. Sihver W, Nordberg A, Langstrom B, et al. Development of ligands for in vivo imaging of cerebral nicotinic receptors. Behav Brain Res 2000;113:143–157.
12. Fujita M, Ichise M, van Dyck CH, et al. Quantification of nicotinic acetylcholine receptors in human brain using [^{123}I]5-I-A-85380 SPET. Eur J Nucl Med 2003;30:1620–1629.
13. Baldwin RM, Zoghbi SS, Staley JK, et al. Chemical composition of ^{123}I-5-IA in baboon brain after intravenous administration. J Nucl Med 2002;43:45P.
14. Kulak JM, Sum J, Musachio JL, et al. 5-Iodo-A-85380 binds to alpha-conotoxin MII-sensitive nicotinic acetylcholine receptors (nAChRs) as well as alpha4beta2* subtypes. J Neurochem 2002;81:403–406.
15. Iida H, Narita Y, Kado H, et al. Effects of scatter and attenuation correction on quantitative assessment of regional cerebral blood flow with SPECT. J Nucl Med 1998;39:181–189.
16. Ichise M, Toyama H, Innis RB, Carson RE. Strategies to improve neuroreceptor parameter estimation by linear regression analysis. J Cereb Blood Flow Metab 2002;22:1271–1281.
17. Ichise M, Fujita M, Zoghbi SS, et al. Parametric imaging of distribution volume and tracer delivery by noise-resistant linear regression analysis: application to [^{123}I]5-I-A-85380 SPECT imaging of a4b2 nicotinic acetylcholine receptors in human. NeuroImage 2004;22:T180–T181.
18. Friston KJ, Holmes AP, Worsley KJ, et al. Statistical parametric maps in functional imaging: a general linear approach. Hum Brain Mapping 1995;2:189–210.
19. Quik M, Bordia T, Okihara M, et al. L-DOPA treatment modulates nicotinic receptors in monkey striatum. Mol Pharmacol 2003;64:619–628.
20. Burton EJ, McKeith IG, Burn DJ, et al. Cerebral atrophy in Parkinson's disease with and without dementia: a comparison with Alzheimer's disease, dementia with Lewy bodies and controls.Brain 2004;127:791–800.

nature medicine

Monolayered mesenchymal stem cells repair scarred myocardium after myocardial infarction

Yoshinori Miyahara[1,9], Noritoshi Nagaya[1,9], Masaharu Kataoka[1], Bobby Yanagawa[1], Koichi Tanaka[1], Hiroyuki Hao[2], Kozo Ishino[3], Hideyuki Ishida[4], Tatsuya Shimizu[5], Kenji Kangawa[6], Shunji Sano[3], Teruo Okano[5], Soichiro Kitamura[7] & Hidezo Mori[8]

Mesenchymal stem cells are multipotent cells that can differentiate into cardiomyocytes and vascular endothelial cells. Here we show, using cell sheet technology, that monolayered mesenchymal stem cells have multipotent and self-propagating properties after transplantation into infarcted rat hearts. We cultured adipose tissue–derived mesenchymal stem cells characterized by flow cytometry using temperature-responsive culture dishes. Four weeks after coronary ligation, we transplanted the monolayered mesenchymal stem cells onto the scarred myocardium. After transplantation, the engrafted sheet gradually grew to form a thick stratum that included newly formed vessels, undifferentiated cells and few cardiomyocytes. The mesenchymal stem cell sheet also acted through paracrine pathways to trigger angiogenesis. Unlike a fibroblast cell sheet, the monolayered mesenchymal stem cells reversed wall thinning in the scar area and improved cardiac function in rats with myocardial infarction. Thus, transplantation of monolayered mesenchymal stem cells may be a new therapeutic strategy for cardiac tissue regeneration.

Myocardial infarction, a main cause of heart failure, leads to loss of cardiac tissue and impairment of left ventricular function. Therefore, restoring the scarred myocardium is desirable for the treatment of heart failure. Although needle injections of bone marrow cells into the myocardium have been performed for cardiac regeneration[1–5], it is difficult to reconstruct sufficient cardiac mass in the thinned scar area after myocardial infarction.

Recently, our colleagues have developed cell sheets using temperature-responsive culture dishes[6]. These cell sheets allow for cell-to-cell connections and maintain the presence of adhesion proteins because enzymatic digestion is not needed[7–10]. Therefore, cell sheet transplantation may be a promising strategy for partial cardiac tissue reconstruction. Skeletal myoblasts, fetal cardiomyocytes and embryonic stem cells have been considered as candidates for an implantable cell source[11–13]. It is difficult, however, to produce a multilayered construct requiring a vascular network. Thus, autologous somatic stem cells with self-propagating properties that can induce angiogenesis are a desirable cell source for a transplantable sheet.

Mesenchymal stem cells (MSCs) are multipotent adult stem cells that reside within the bone marrow microenvironment[14,15]. MSCs can differentiate not only into osteoblasts, chondrocytes, neurons and skeletal muscle cells, but also into vascular endothelial cells[16] and cardiomyocytes[17–20]. In contrast to their hematopoietic counterparts, MSCs are adherent and can expand in culture. Recently, MSCs have been isolated from adipose tissue[21–24], which is typically abundant in individuals with cardiovascular disease. Here, we investigated the therapeutic potency of monolayered MSCs derived from adipose tissue using cell sheet technology.

RESULTS

Characteristics of adipose tissue–derived MSCs

We isolated MSCs from subcutaneous adipose tissue of male Sprague-Dawley rats on the basis of the adherent properties of these cells. We obtained $1.7 \times 10^5 \pm 0.2 \times 10^5$ cells from 1 g adipose tissue in a 12-h culture. By day 4 of culture of the minced adipose tissue, spindle-shaped adherent cells were apparent and formed symmetric colonies. After approximately three to four passages, most adherent cells expressed CD29 and CD90 (**Supplementary Fig. 1** online). In contrast, the majority of adherent cells were negative for CD34 and CD45. They were also negative for CD31, a marker for vascular endothelial cells, and negative for α smooth muscle actin (αSMA), a marker for smooth muscle cells. A small fraction of adherent cells expressed CD71, CD106 and CD117. These results were similar to those from bone marrow–derived MSCs[15,22,25] (**Supplementary Fig. 1** online). Using previously described methods[16,22,26], we confirmed that these adipose-derived adherent cells, like bone marrow–derived MSCs, were multipotent, as judged by their ability to differentiate into adipocytes, osteoblasts and vascular endothelial cells. Thus, we

[1]Department of Regenerative Medicine and Tissue Engineering, National Cardiovascular Center Research Institute and [2]Department of Pathology, National Cardiovascular Center, 5-7-1 Fujishirodai, Suita, Osaka, 565-8565, Japan. [3]Department of Cardiovascular Surgery, Okayama University Graduate School of Medicine, Dentistry and Pharmaceutical Sciences, 2-5-1 Shikata-cho, Okayama, 700-8555, Japan. [4]Department of Physiology, School of Medicine, Tokai University, Bohseidai, Isehara, Kanagawa, 259-1193, Japan. [5]Institute of Advanced Biomedical Engineering and Science, Tokyo Woman's Medical University, 8-1 Kawada-cho, Shinjuku-ku, Tokyo, 162-8666, Japan. [6]Department of Biochemistry, National Cardiovascular Center Research Institute and [7]Department of Cardiovascular Surgery, National Cardiovascular Center and [8]Department of Cardiac Physiology, National Cardiovascular Center Research Institute, 5-7-1 Fujishirodai, Suita, Osaka, 565-8565, Japan. [9]These authors contributed equally to this work. Correspondence should be addressed to N.N. (nnagaya@ri.ncvc.go.jp) or H.M. (hidemori@ri.ncvc.go.jp).

Received 9 August 2005; accepted 3 March 2006; published online 2 April 2006; doi:10.1038/nm1391

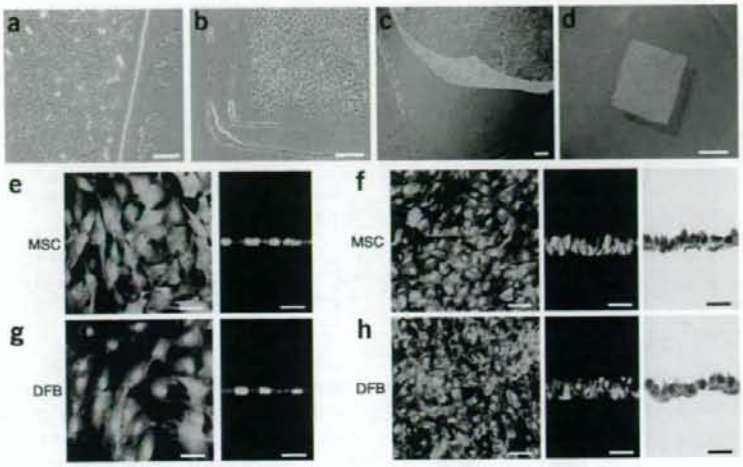

Figure 1 Preparation of monolayered MSCs. (**a**) MSCs 2 d after seeding on a temperature-responsive dish. (**b**) Cultured MSCs expanded to confluence within the square area of the dish by day 3. (**c**) The monolayered MSCs detached easily from the culture dish at 20 °C. (**d**) The completely detached monolayered MSCs were identified as a 12 × 12 mm square sheet. (**e–h**) Cross-sectional analysis of GFP-expressing monolayered MSCs and DFBs before detachment (**e** and **g**, confocal images) and after detachment (**f** and **h**, left and center, confocal images; right, Masson trichrome). The thickness of both monolayers was 3.5-fold greater than the thickness before detachment, and constituent cells were compacted. Scale bars in **a–c**, 100 μm; in **d**, 5 mm; in **e–h**, 20 μm.

confirmed that the majority of adherent cells isolated from adipose tissue were MSCs.

Preparation and transplantation of monolayered MSCs

We cultured adipose tissue–derived MSCs (5×10^5 cells) on temperature-responsive dishes for 3 d until confluent. MSCs were attached on the poly-*N*-isopropylacrylamide (PIPAAm)-grafted area (24 × 24 mm; **Fig. 1a,b**). As the culture temperature was decreased from 37 °C to 20 °C, MSCs detached spontaneously and floated up into the culture medium as a monolayer of MSCs within 40 min (**Fig. 1c,d**). As a control, we prepared dermal fibroblasts (DFBs) by the skin explant technique[27]. DFBs (8×10^5 cells) were cultured on the temperature-responsive dishes, and monolayered DFBs were fabricated as described above. The final cell counts for monolayered MSCs and DFBs before transplantation were $9.4 \pm 0.6 \times 10^5$ and $8.6 \pm 0.6 \times 10^5$ cells, respectively ($n = 6$ each). To identify the thickness of monolayered MSCs, we used green fluorescent protein (GFP)-expressing cell grafts derived from the GFP-transgenic Sprague-Dawley rats. Immediately after detachment, cells became compacted, possibly owing to cytoskeletal tensile reorganization, and the thickness of monolayered MSCs and DFBs was approximately 3.5-fold greater than the thickness before detachment (MSCs, 6.2 ± 0.3 to 21.5 ± 0.8 μm; DFBs, 6.5 ± 0.4 to 22.4 ± 1.1 μm; **Fig. 1e–h**). MSCs on the temperature-responsive dishes were positive for vimentin and slightly positive for collagen type 1, whereas DFBs were positive for both markers (**Fig. 2a**). We transferred detached monolayered MSCs above the myocardial scar (**Fig. 2b**) and then attached them to the surface of the anterior scar (**Fig. 2c**).

Secretion of angiogenic factors from monolayered MSCs

We measured secretion of angiogenic factors from MSCs 24 h after monolayers had formed, equivalent to day 4 after initial cell seeding. The monolayered MSCs secreted significantly larger amounts of angiogenic and antiapoptotic factors such as vascular endothelial growth factor (VEGF) and hepatocyte growth factor (HGF) than did the monolayered DFBs ($P < 0.01$; **Fig. 2d**). The control medium supplemented with 10% fetal calf serum contained less than 5 pg/ml of VEGF or HGF. These results suggest that the paracrine effects of monolayered MSCs on host myocardium are greater than those of monolayered DFBs.

Engraftment and growth of monolayered MSCs

To identify the transplanted cells in myocardial sections, we used GFP-expressing cell grafts derived from the GFP-transgenic Sprague-Dawley rats. We grafted monolayered MSCs or DFBs onto the scar area of the anterior wall (**Fig. 3**). Fluorescence microscopy showed that GFP-expressing monolayered MSCs gradually grew *in situ* and developed into a thick stratum, up to ~600 μm thick over the native tissue at 4 weeks (**Fig. 3a–f**). The engrafted MSC tissue tapered off toward the healthy myocardium (**Fig. 3d,e**), although most of the monolayered MSCs were attached only to the scar area in the anterior wall because of the large infarct. We rarely detected TUNEL-positive MSCs in the sheet (<1%) 48 h after transplantation (**Fig. 3g**), implying that cell viability in the sheet was maintained. In contrast, we frequently detected TUNEL-positive cells (15% ± 2%) in the DFB sheet, which was observed as a thin layer above the scar. Subsequently, the DFB sheet was undetectable 1 week later. Masson trichrome staining showed increased thickness of the anterior wall and attenuation of left ventricle enlargement after transplantation of monolayered MSCs (**Fig. 3h**), although the infarct size did not differ significantly among the untreated, DFB and MSC groups (**Supplementary Table 1** online).

Reconstruction of cardiac mass

After growth *in situ*, GFP-expressing MSC tissue contained a number of mature vascular structures that had positive staining for von Willebrand factor (vWF) and αSMA (**Fig. 4a,b**). A small fraction of the MSC tissue had positive staining for cardiac troponin T and desmin (**Fig. 4c,d**). On the other hand, a large proportion of the MSC tissue was positive for vimentin, a marker for mesenchymal lineage cells (**Fig. 4e**). The percentages of graft-derived cells that expressed endothelial (vWF), smooth muscle (αSMA), cardiac (troponin T) and mesenchymal (vimentin) markers were 12.2% ± 0.6%, 5.0% ± 0.3%, 5.3% ± 0.3% and 57.8% ± 2.2%, respectively. Notably, based on expression of these markers, two-thirds of vascular endothelial cells, four-fifths of smooth muscle cells and one-twentieth of cardiomyocytes within the MSC tissue were GFP^- and hence were derived from the host. The MSC tissue stained modestly for collagen type 1 (**Fig. 4f**). Picrosirius red staining showed that collagen deposition was found mainly in the extracellular matrix and the epicardial margin of the MSC tissue (**Fig. 4g**). Excluding staining in blood vessels, the MSC tissue was also negative for αSMA, a marker for myofibroblasts (**Fig. 4b**). This phenotype was consistent with properties of MSCs

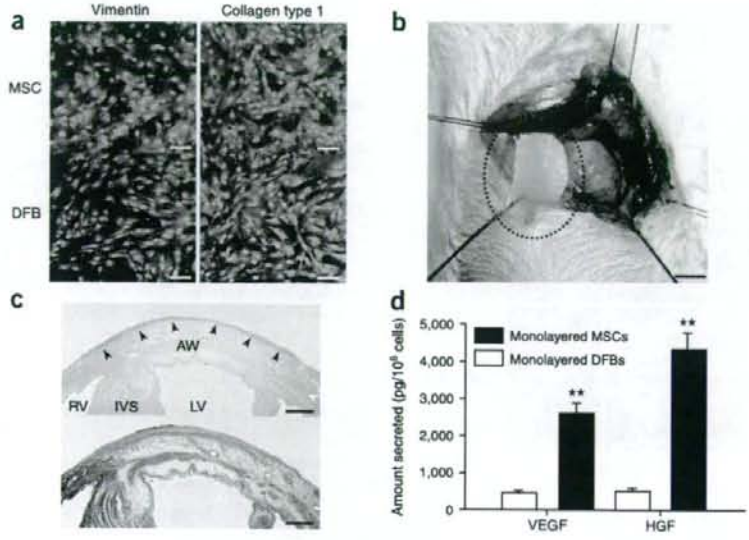

Figure 2 Characteristics of monolayered MSCs. (**a**) Properties of constituent cells in the monolayered grafts. Compared with DFBs (green), MSCs (green) are positive for vimentin (red) and slightly positive for collagen type 1 (red). (**b**) Monolayered MSCs (in the dotted circle) transferred to the infarcted heart. (**c**) Extent of monolayered MSCs 48 h after transplantation (arrows). AW, anterior wall; LV, left ventricle; RV right ventricle; IVS, interventricular septum. (**d**) Comparison of secretion of growth factors between monolayered MSCs and DFBs. $^{**}P < 0.01$ versus DFBs. Scale bar in **a**, 20 μm; in **b**, 5 mm; in **c**, 100 μm.

before transplantation (**Fig. 2a** and **Supplementary Fig. 1** online), suggesting that the MSC tissue includes a number of undifferentiated MSCs. Taken together, the grown MSC tissue was composed of newly formed blood vessels, undifferentiated MSCs and few cardiomyocytes.

Fluorescence *in situ* hybridization analysis

We performed fluorescence *in situ* hybridization (FISH) to detect X and Y chromosomes after sex-mismatched transplantation of monolayered MSCs. We transplanted GFP-expressing monolayered MSCs derived from male rats to female Sprague-Dawley rats that had suffered an infarct. Four weeks later, newly formed cardiomyocytes that were positive for GFP had only one set of X and Y chromosomes, whereas we detected two X chromosomes exclusively in GFP^- host-derived cells (**Fig. 4h**). We counted the X and Y chromosomes in male and female control rats and in the MSC sheet–transplanted rats (**Supplementary Table 2** online), and we did not detect extra copies of the X or Y chromosome in graft-derived GFP^+ cardiomyocytes. When we compared the frequencies of the occurrence of zero, one, two and more than two X chromosomes in the GFP^+ cardiomyocytes with the frequencies in male control cardiomyocytes, the GFP^+ cardiomyocytes did not show an increased proportion of X chromosomes ($0.25 > P > 0.10$, χ^2 test).

Effects of monolayered MSCs on cardiac function

Heart failure developed 8 weeks after coronary ligation, as indicated by an increase in left ventricle end-diastolic pressure (LVEDP) and attenuation of maximum and minimum rate of change in left ventricular pressure (dP/dt). Autologous transplantation of monolayered MSCs, however, resulted in decreased LVEDP (**Fig. 5a**). Left ventricle maximum and minimum dP/dt were significantly improved in the MSC group (**Fig. 5b,c**). We did not observe these hemodynamic improvements in the DFB group. The MSC group also had significantly lower right ventricular weight and lung weight than the DFB and untreated groups 4 weeks after transplantation (**Supplementary Table 1** online). These results suggest that transplantation of monolayered MSCs has beneficial hemodynamic effects in rats with chronic heart failure.

Echocardiographic analysis showed that transplantation of monolayered MSCs significantly increased diastolic thickness of the infarcted anterior wall (**Fig. 5d**). Left ventricle end-diastolic dimension at 8 weeks was significantly smaller in the MSC group than in the DFB and untreated groups (**Fig. 5e**). Transplantation of the monolayered MSCs significantly increased left ventricle fractional shortening (**Fig. 5f**). Left ventricle wall stress in diastole was markedly lower in the MSC group than in the DFB and untreated groups (**Supplementary Table 3** online). Plasma atrial natriuretic peptide (ANP) in the DFB and untreated groups was markedly elevated 8 weeks after myocardial infarction (**Fig. 5g**). Transplantation of the monolayered MSCs inhibited the increase in plasma ANP.

Survival analysis

The Kaplan-Meier survival curve showed that 4-week survival after coronary ligation did not differ significantly between the untreated and MSC groups before transplantation (**Fig. 5h**). Notably, however, no rats died after transplantation of monolayered MSCs. Therefore, the survival rate after transplantation was markedly higher in the MSC group than in the untreated group (4-week survival after transplantation was 100% for the MSC group versus 71% for the untreated group, log-rank test, $P < 0.05$).

DISCUSSION

There are several advantages to monolayered MSC transplantation. First, the self-propagating property of MSCs *in situ* leads to the formation of a thick stratum on the surface of the scarred myocardium. Second, the multipotency of MSCs and their ability to supply angiogenic cytokines allows neovascularization in the MSC tissue. Third, the reconstruction of thick myocardial tissue reduces left ventricle wall stress and results in improvement of cardiac function after myocardial infarction. Finally, a substantial part of the transplanted tissue is composed of undifferentiated MSCs, and it is tempting to speculate that such cells may act against future progressive left ventricle remodeling.

Cellular cardiomyoplasty using needle injections is emerging as a treatment option for individuals with chronic heart failure, but it may be limited by failure to regenerate cardiac mass. The cell sheet allows for cell-to-cell connections owing to the lack a need for enzymatic digestion[6–10]. Thus, the cell sheet has attracted considerable interest as a tool for tissue engineering[28]. Here, we used adipose tissue–derived MSCs as a cellular source for the cell sheet, which resulted in successful autologous transplantation in heterogenic rats without immunological